parallel to the vortex axis. k_F is the Fermi momentum. At small n, the decay length becomes much larger than the coherence length.

We now consider the ballistic conductance of the vortex of the length L. Consider the superconducting disk with the vortex as placed between the two normal metal reservoirs. Each quasiparticle mode contribution into the conductance is proportional to $(e^2/\hbar)\exp(-2\gamma_n L)$. Then the total conductance due to single-particle tunnelling processes becomes:

$$G \propto \frac{e^2}{\hbar} T_b \sum_{\mu} \sum_{n=n_{min}}^{n_{max}} \exp(-2\gamma_n L) \qquad (3)$$

where $n_{min} \approx \mu$, $n_{max} \approx k_F\xi$. We have assumed here the barrier transmission probability T_b to be the same for all channels (in a more detailed model, this coefficient should depend on the quantum numbers). In the case of interest we focus on, $\xi < L < k_F\xi^2$. Replacing sums over μ and n by the integrals, we arrive at the final estimate:

$$G \propto \frac{e^2}{\hbar} T_b (k_F\xi)^2 \frac{\xi^2}{L^2} \qquad (4)$$

For small samples of the size of several coherence lengths, single-particle conductance compares favourably with the two-particle Andreev contribution ($\propto T_b^2$). At large distances, $L > k_F\xi^2$, the $1/L^2$ power-law decay of the conductance crosses over to the exponential reduction $\propto \exp[-L/k_F\xi^2)]$, and in the long samples the single-particle current through the vortex channels is shunted by the supercurrent through the borders of the vortex core.

For the schematic experimental design shown in Fig. 1, we see that there is a notable dependence of the ballistic conductance behaviour on the magnetic field that exists at the area of the contact. For large-area contacts, all the additional channels—corresponding to new maxima of the DOS—that appear as flux quanta subsequently enter the disk, contributing to the conductivity. Hence such a 'large-contact-area device' will exhibit a step-like growth of conductance with increasing magnetic field (see Fig. 1). On the contrary, a point contact with an area much smaller than the area of the vortex core feels the density of states just at its location, and thus shows a strong dependence of the transmission probability T_b on μ and on contact position. Placing the point contact strictly at the centre of the disk, we observe either nearly zero (for even m, where the central spot in the DOS is absent) or finite alternating conductance for odd m, where single-particle tunnelling occurs via the central peak (see Fig. 1). This alternating conductance realizes a quantum switch, with magnetic field playing the role of gate voltage. Generally, the magnetic-field dependence of conductance will exhibit a mixture of the above step-like and alternating behaviours.

The ballistic contribution to the conductance dominates the quasiparticle transport at rather low temperatures, $T < \Delta\xi/L$; in all other cases, the conductance will be determined by the thermodynamically averaged DOS. Thus, experimental realization of ballistic quantum switch regime requires low temperatures—and pure, thin samples. □

Received 16 August; accepted 7 November 2001.

1. Boato, G. *et al.* Direct evidence for quantized flux threads in type II superconductors. *Solid State Commun.* **3,** 173–176 (1965).
2. McLachlan, D. S. Quantum oscillations and the order of the phase charge in a low k type II superconducting microcylinder. *Solid State Commun.* **8,** 1589–1593 (1970).
3. Geim, A. K. *et al.* Fine structure in magnetization of individual fluxoid states. *Phys. Rev. Lett.* **85,** 1528–1531 (2000).
4. Schweigert, V. A., Peeters, F. M. & Deo, P. S. Vortex phase diagram for mesoscopic superconducting disks. *Phys. Rev. Lett.* **81,** 2783–2786 (1998).
5. Chibotaru, L. F. *et al.* Symmetry-induced formation of antivortices in mesoscopic superconductors. *Nature* **408,** 833–835 (2000).
6. Giaever, I. in *Tunneling Phenomena in Solids* (eds Burstein, E. & Lundqvist, S.) 255–271 (Plenum, New York, 1969).
7. Caroli, C., de Gennes, P. G. & Matricon, J. Bound fermion states on a vortex line in a type II superconductor. *Phys. Lett.* **9,** 307–309 (1964).
8. Volovik, G. E. Vortex motion in Fermi superfluids and the Callan-Harvey effect. *JETP Lett.* **57,** 244–246 (1993).
9. Tanaka, Y. *et al.* Energy spectrum of the quasiparticle in a quantum dot formed by a superconducting pair potential under a magnetic field. *Solid State Commun.* **85,** 321–326 (1993).
10. Virtanen, S. M. M. & Salomaa, M. M. Multiquantum vortices in superconductors: Electronic and scanning tunneling microscopy spectra. *Phys. Rev. B* **60,** 14581–14584 (1999).
11. Hess, H. F. *et al.* Scanning-tunneling-microscope observation of the Abrikosov flux lattice and the density of states near and inside a fluxoid. *Phys. Rev. Lett.* **62,** 214–217 (1989).
12. Pincus, P. Magnetic-field-induced surface states in a pure type-I superconductor. *Phys. Rev. B* **158,** 346–353 (1967).
13. Azbel', M. Ya. & Blank, A. Ya. Magnetic surface levels in superconductors. *JETP Lett.* **10,** 32–35 (1969).

Acknowledgements

We thank G. Crabtree, G. Karapetrov, A. Koshelev, V. Moshchalkov, D. A. Ryzhov, S. V. Sharov, I. A. Shereshevsky and I. D. Tokman for discussions. This work was supported by the US DOE Office of Science, a NATO Collaborative Linkage Grant, and by the Russian Foundation for Fundamental Research.

Correspondence and requests for materials should be addressed to V.M.V. (e-mail: vinokur@msd.anl.gov).

A robust DNA mechanical device controlled by hybridization topology

Hao Yan, Xiaoping Zhang, Zhiyong Shen & Nadrian C. Seeman

Department of Chemistry, New York University, New York, New York 10003, USA

Controlled mechanical movement in molecular-scale devices has been realized in a variety of systems—catenanes and rotaxanes[1–3], chiroptical molecular switches[4], molecular ratchets[5] and DNA[6]—by exploiting conformational changes triggered by changes in redox potential or temperature, reversible binding of small molecules or ions, or irradiation. The incorporation of such devices into arrays[7,8] could in principle lead to complex structural states suitable for nanorobotic applications, provided that individual devices can be addressed separately. But because the triggers commonly used tend to act equally on all the devices that are present, they will need to be localized very tightly. This could be readily achieved with devices that are controlled individually by separate and device-specific reagents. A trigger mechanism that allows such specific control is the reversible binding of DNA strands, thereby 'fuelling' conformational changes in a DNA machine[9]. Here we improve upon the initial prototype system that uses this mechanism but generates by-products[9], by demonstrating a robust sequence-dependent rotary DNA device operating in a four-step cycle. We show that DNA strands control and fuel our device cycle by inducing the interconversion between two robust topological motifs, paranemic crossover (PX) DNA[10,11] and its topoisomer JX_2 DNA, in which one strand end is rotated relative to the other by 180°. We expect that a wide range of analogous yet distinct rotary devices can be created by changing the control strands and the device sequences to which they bind.

PX DNA (Fig. 1a, left) is a four-stranded molecule in which two parallel double helices are joined by reciprocal exchange (crossing over) of strands at every point where the strands come together[10,11]. JX_2 (Fig. 1a, right) is a topoisomer of PX DNA that contains two adjacent sites where backbones juxtapose without crossing over. The colour coding of the strands and labels in Fig. 1 indicates that the top ends, A and B, are the same in both molecules, but the bottom ends, C and D, are rotated 180°. This rotation is the basis for the operation of the device. We have used strand replacement[9] to interconvert the PX and JX_2 motifs.

In the device that we have constructed, one strand of each of the blue and red strand pairs is broken into three strands. The principles of operation are illustrated in Fig. 1b, where the red and blue strands of opposite polarity are shown connected by hairpin loops. Thus, the PX molecule shown there consists of one red strand, one blue strand, and two green strands, termed the 'set' strands, because they set the state of the device to be in the PX conformation; similarly, the JX_2 molecule has purple set strands. The set strand associated with the red strand has a 5′ single-stranded extension, and the set strand associated with the blue strand has a similar 3′ extension. Extensions like these can[9] be used to initiate branch migration that leads to removal of the strand from the branched motif, because it is paired with a complementary strand along its entire length. Thus, a complement to the entire length of the set strand (termed a 'fuel' strand) will pair with it in preference to the partially paired set strand in the PX (or JX_2) motif.

Process I (Fig. 1b) shows the addition of fuel strand complements to the two green set strands of the PX device, producing the unstructured intermediate at the top of the drawing. Process II shows the addition of pale-purple set strands that convert the intermediate to the JX_2 conformation. Process III shows the addition of fuel strands that convert the JX_2 molecule to the unstructured intermediate, and process IV shows the addition of the green set strands to produce the PX conformation again. Alternation between a paired structure and a partially unpaired structure analogous to this intermediate characterized the action of the system of ref. 9. In the device described here, the four-step cycle leads to two robust end points, the PX state and the JX_2 state.

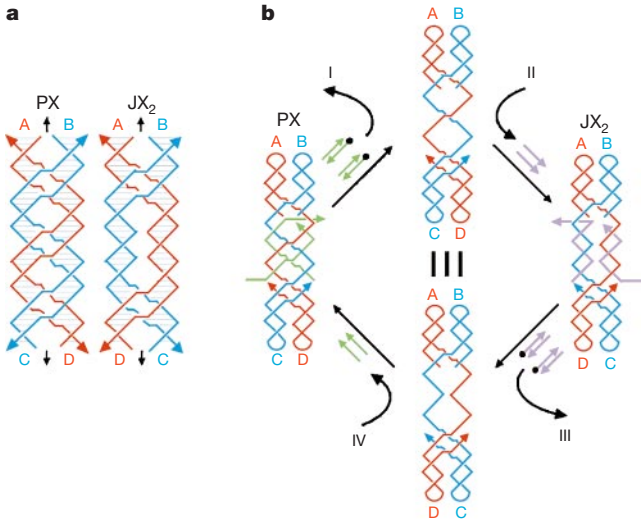

Figure 1 Schematic drawings of the device. **a**, The PX and JX_2 motifs. The PX motif, postulated to be involved in genetic recombination[11], consists of two helical domains formed by four strands that flank a central dyad axis (indicated by the vertical black arrows). Two strands are drawn in red and two in blue, where the arrowheads indicate the 3′ ends of the strands. The Watson–Crick base pairing in which every nucleotide participates is indicated by the thin horizontal lines within the two double helical domains. Every possible crossover occurs between the two helical domains. The same conventions apply to the JX_2 domain, which lacks two crossovers in the middle. The letters A, B, C and D, along with the colour coding, show that the bottom of the JX_2 motif (C and D) are rotated 180° relative to the PX motif. **b**, Principles of device operation. On the left is a PX molecule. The green set strands are removed by the addition of biotinylated green 'fuel' strands (biotin indicated by black circles) in process I. The unstructured intermediate is converted to the JX_2 motif by the addition of the pale-purple set strands in process II. The JX_2 molecule is converted to the unstructured intermediate by the addition of biotinylated pale-purple 'fuel' strands in process III. The identity of this intermediate and the one above it is indicated by the identity symbol between them. The cycle is completed by the addition of green set strands in process IV, restoring the PX device.

To demonstrate the operation of a robust molecular mechanical device, it is necessary to show both the uniform behaviour of the bulk material, and also to visualize the structural transformations of selected molecules. Figure 2a illustrates the formation and interconversion of both PX and JX_2 DNA by non-denaturing gel electrophoresis. All experiments are performed in a buffer containing 40 mM Tris·HCl, pH 8.0, 20 mM acetic acid, 2 mM EDTA and 12.5 mM magnesium acetate; sequences of all molecules used are in the Supplementary Information. The absence of species other than the PX or JX_2 molecules (for example, the dimers noted by Yurke *et al.*[9], or potential dissociation products) attests to the robustness of the device in bulk. Figure 2b illustrates the cycling of the device between the PX and JX_2 states. The right portion of Fig. 2b shows five steps of operation, beginning in the JX_2 state; the left portion shows five steps that begin from the PX state. The intermediate structure is stable at the highest temperatures (20 °C) to which the device has been subjected in this experiment (see Supplementary Information).

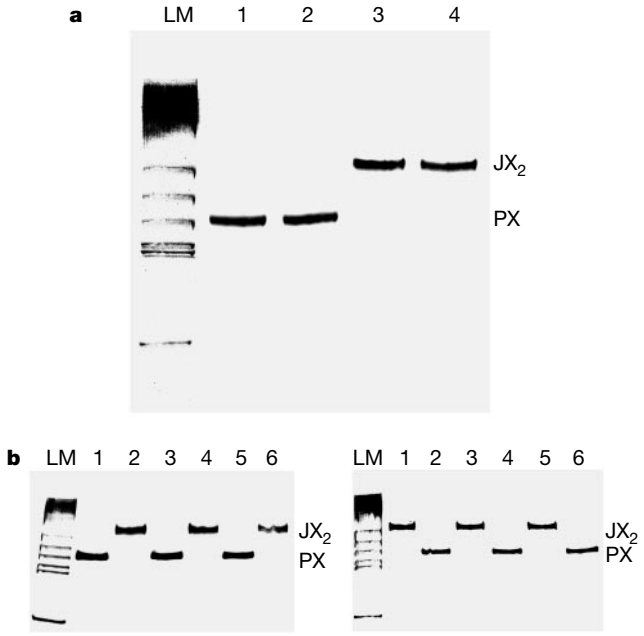

Figure 2 Gel evidence for the operation of the device. **a**, The components of the device in operation. This is a 14% non-denaturing polyacrylamide gel, run at 20 °C and stained with stains-all dye (Sigma E-7762). The lane LM contains linear length markers derived from *Hae*III digestion of pBR322. Device strand sequences have been designed using the program SEQUIN[13], synthesized by routine phosphoramidite techniques[14] and gel purified. Strands are hybridized at 90 °C (5 min), 65 °C (15 min), 45 °C (30 min), 37 °C (20 min) and 20 °C (30 min). Lane 1 contains the device [1 μM] assembled with PX set strands and lane 4 contains the device [1 μM] assembled with JX_2 set strands. Gel mobilities differ because the PX device is likely to have a more compact time-averaged structure than the JX_2 device[15]. Lane 2 contains the products of removing the JX_2 set strands from the material in lane 4 and replacing them with set strands corresponding to the PX conformation. Likewise, lane 3 contains the products of removing the PX set strands from the material in lane 1 and replacing them with those corresponding to the JX_2 conformation. Note the absence of extraneous products in lanes 2 and 3, indicating the robustness of these transformations. **b**, Cycling the device. The two portions of this panel show the cycling of the device through 5 steps. Lane 1 is the initial conformation (JX_2 right and PX left), and lanes 2 to 6, respectively, show alternating transformations to the other state. Fuel strands were added to the preformed PX or JX_2 at 20 °C and kept at 20 °C for 60 min; the mixture was treated with streptavidin beads at 20 °C for 30 min to remove the set-strand/fuel-strand duplexes. After removing the set strands of PX or JX_2, the set strands of JX_2 or PX molecules were added to the solution and kept at 20 °C for 60 min to establish the device conformation. The addition of fuel strands, followed by set strands, was then repeated three times.

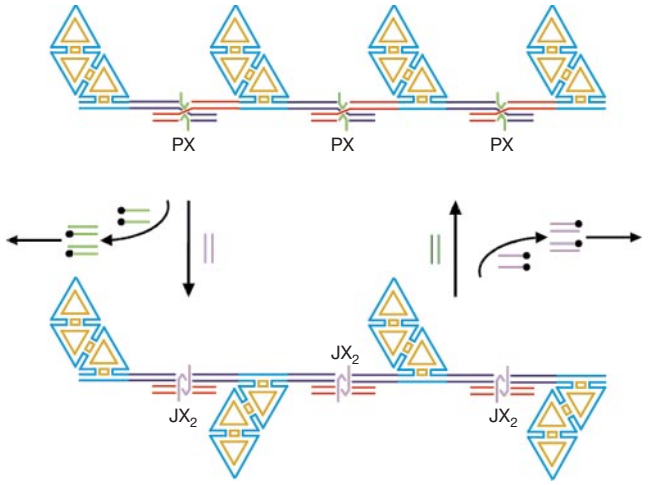

Figure 3 A highly simplified representation of the system used. It consists of a one-dimensional array of half-hexagons (light-blue outer strands, ochre inner strands) joined by the device. Each half-hexagon consists of three edge-sharing DNA triangles[16] whose edges are three turns long; the edge-sharing structure is a DNA double crossover molecule[12], which also attaches the half-hexagon to the linear components of the array. The colour coding in the vicinity of the device has been retained from Fig. 1, with green set strands in the PX state, pale-purple set strands in the JX_2 state and constant strands in red and blue; the actual strand structure is both more complex and larger than the structure in Fig. 2, and is shown in detail with its sequence in the Supplementary Information. There are 39 nucleotides between the first device crossover point and the nearest triangle crossover point, a number that was determined empirically to give the most nearly planar structure, although it represents four turns of DNA. In the upper molecule, all of the half-hexagons are aligned pointing in the same direction (*cis*), whereas they point in opposite directions in the bottom molecule (*trans*). Biotinylated fuel strands (with black filled circles) are shown removing set strands in both parts of the cycle. Note that relative to the half-hexagon on the left, the third one has rotated 360° and the rightmost one has rotated 540°.

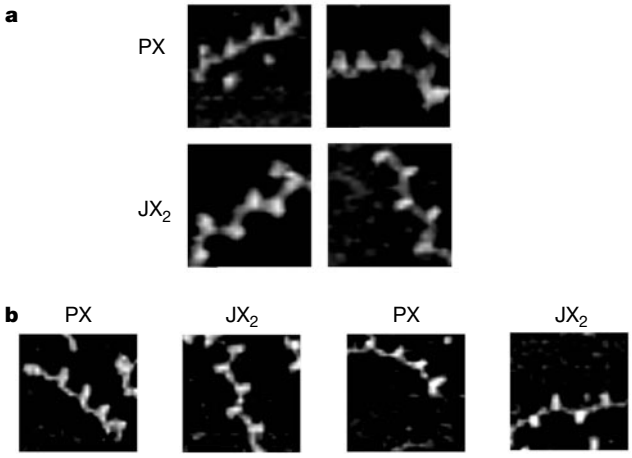

Figure 4 Evidence for the operation of the device, obtained from atomic force microscopy (AFM). All initial species are produced by heating their constituent single strands in boiling water and then cooling in a styrofoam box over a period of 2 days. The one-dimensional arrays of these half-hexagon-plus-device units cohere by way of 8-nucleotide sticky ends. Non-denaturing gels demonstrate the resistance of this sticky end to disruption at 45 °C, where these conversions were performed (see Supplementary Information). **a**, Control images. These images contain control molecules, not devices, that are constrained to be in the PX or JX_2 motifs. AFM samples are prepared by placing 1 μl of solution on a piece of freshly cleaved mica (Ted Pella, Inc.), blowing it dry, and washing several times with distilled water. Images are obtained in isopropanol by scanning with a Nanoscope II in contact mode. The upper panels show PX linear arrays in a *cis* arrangement, and the lower panels show JX_2 linear arrays in a *trans* arrangement. **b**, Cycling of the device. This panel shows three steps of the operation of the device, sampling aliquots from each cycle. The system originates in the PX state, and is then converted (left to right) to the JX_2 state, back to PX, and then back to JX_2. The PX linear arrays are clearly in the *cis* arrangement, and the JX_2 linear arrays are clearly in the *trans* arrangement. All images show an area 200 nm × 200 nm.

Altered gel mobilities do not guarantee that the construct undergoes the designated structural transformation. We demonstrate this aspect of the device with the system shown in Fig. 3. We have constructed half-hexagon markers via edge-sharing between three triangles; each of the shared edges is a DNA double crossover molecule[12]. The half-hexagons are connected into one-dimensional oligomeric arrays by linkage through extensions that include PX-JX_2 devices. Figure 3a shows that if the devices are all in the PX state, the half-hexagons have a *cis* arrangement, where they all point in the same direction. However, when the devices are all in the JX_2 state, the half-hexagons form a zigzag *trans* structure.

Figure 4 illustrates the operation of the device, using atomic force microscopy (AFM) images. Figure 4a shows two examples for the *cis* and *trans* systems of Fig. 3, but containing links that are fixed to be PX or JX_2 molecules, rather than PX-JX_2 devices. The PX state contains a series of half-hexagons extended in a parallel direction, much like the extended fingers of a hand. By contrast, the JX_2 state is characterized by a zigzag arrangement of the half-hexagon extensions. Figure 4b illustrates the operation of the device by displaying representative molecules sampled from solutions expected to contain successively (left to right) PX, JX_2, PX and JX_2, states, as the system is cycled. The PX molecules have their half-hexagon markers aligned in a *cis* arrangement, whereas the markers in the JX_2 molecules are all *trans*. Thus, the system operates as designed, both in bulk and in individual cases. The intermediate state produces a single band on a gel, but it is not well-structured when examined by AFM (data not shown).

We have shown that a rotary nanomechanical device is capable of being cycled by the addition of strands that direct its structure; we describe the system as robust, because both end points—the PX state and the JX_2 state—are well-defined structures that lack single-stranded regions in structural roles. The extent of motion produced within the rotary device itself will be a function of the distance from its midline, ranging from about 0.4 to 4 nm; however, motions as large as 35 nm have been achieved with the half-hexagon array. Multiple species could be obtained by changing the set strands and the sequences to which they bind. If N different device species of this type can be incorporated into two-dimensional[7,8] or three-dimensional crystalline arrays, 2^N different structural states will be available to the system. Multiple robust states of this sort are necessary for an effective nanorobotics, so that a diversity of shapes can be programmed. Further experimentation will be required to establish that this DNA device can transmit a force capable of performing useful work on other chemical species. □

Received 26 April; accepted 8 November 2001.

1. Pease, A. R. *et al.* Switching devices based on interlocked molecules. *Acc. Chem. Res.* **34,** 433–444 (2001).
2. Jimenez, M. C., Dietrich-Buchecker, C. & Sauvage, J.-P. Towards synthetic molecular muscles: contraction and stretching of a linear-rotaxane dimer. *Angew. Chem. Int. Edn Engl.* **39,** 3284–3287 (2000).
3. Brouwer, A. M. *et al.* Photoinduction of fast, reversible translational motion in a hydrogen-bonded molecular shuttle. *Science* **291,** 2124–2128 (2001).
4. Koumura, N., Zijlstra, R. W. J., van Delden, R. A., Harada, N. & Feringa, B. L. Light-driven monodirectional molecular rotor. *Nature* **401,** 152–155 (1999).
5. Kelly, T. R., De Silva, H. & Silva, R. A. Unidirectional rotary motion in a molecular system. *Nature* **401,** 150–152 (1999).
6. Mao, C., Sun, W., Shen, Z. & Seeman, N. C. A DNA nanomechanical device based on the B-Z transition. *Nature* **397,** 144–146 (1999).
7. Winfree, E., Liu, F., Wenzler, L. A. & Seeman, N. C. Design and self-assembly of two-dimensional DNA crystals. *Nature* **394,** 539–544 (1998).
8. LaBean, T. H. *et al.* The construction, analysis, ligation and self-assembly of DNA triple crossover complexes. *J. Am. Chem. Soc.* **122,** 1848–1860 (2000).

9. Yurke, B., Turberfield, A. J., Mills, A. P. Jr, Simmel, F. C. & Neumann, J. L. A DNA-fuelled molecular machine made of DNA. *Nature* **406,** 605–608 (2000).
10. Seeman, N. C. DNA nicks and nodes and nanotechnology. *Nano Lett.* **1,** 22–26 (2001).
11. Shen, Z. *DNA Polycrossover Molecules and their Applications in Homology Recognition.* Thesis, New York Univ. (1999).
12. Fu, T.-J. & Seeman, N. C. DNA double crossover structures. *Biochemistry* **32,** 3211–3220 (1993).
13. Seeman, N. C. De novo design of sequences for nucleic acid structure engineering. *J. Biomol. Struct. Dyn.* **8,** 573–581 (1990).
14. Caruthers, M. H. Gene synthesis machines: DNA chemistry and its uses. *Science* **230,** 281–285 (1985).
15. Sun, W., Mao, C., Iwasaki, H., Kemper, B. & Seeman, N. C. No braiding of Holliday junctions in positively supercoiled DNA molecules. *J. Mol. Biol.* **294,** 683–699 (1999).
16. Yang, X., Wenzler, L. A., Qi, J., Li, X. & Seeman, N. C. Ligation of DNA triangles containing double crossover molecules. *J. Am. Chem. Soc.* **120,** 9779–9786 (1998).

Supplementary Information accompanies the paper on *Nature*'s website (http://www.nature.com).

Acknowledgements

We thank R. Sha for discussions. This work was supported by the Office of Naval Research, the National Institute of General Medical Sciences, the National Science Foundation/ DARPA, the Information Directorate of the Air Force Research Laboratory located at Rome, New York, and the National Science Foundation.

Correspondence and requests for materials should be addressed to N.C.S. (e-mail: ned.seeman@nyu.edu).

Evolutionary speed limits inferred from the fossil record

James W. Kirchner

Department of Earth and Planetary Science, University of California, Berkeley, California 94720-4767, USA

The dynamics of extinction and diversification determine the long-term effects of extinction episodes[1]. If rapid bursts of extinction are offset by equally rapid bursts of diversification, their biodiversity consequences will be transient. But if diversification rates cannot accelerate rapidly enough, pulses of extinction will lead to long-lasting depletion of biodiversity[2,3]. Here I use spectral analysis of the fossil record to test whether diversification rates can accelerate as much as extinction rates, over both short and long spans of geological time. I show that although the long-wavelength variability of diversification rates equals or exceeds that of extinctions, diversification rates are markedly less variable than extinction rates at wavelengths shorter than roughly 25 million years. This implies that there are intrinsic speed limits that constrain how rapidly diversification rates can accelerate in response to pulses of extinction.

To measure how fossil extinction and origination rates fluctuate across different timescales, I used spectral analysis methods[4,5] specially designed for unevenly spaced data such as the fossil record. Spectral analysis decomposes a time series into its component frequencies and measures each of their amplitudes (expressed as their square, the spectral power). My source data are Sepkoski's compilations of Phanerozoic fossil marine animal families[6] and genera[7]. Because the suitability of different extinction and origination metrics is sometimes disputed[8,9], I analysed all four that are in common use: (1) counts of first or last occurrences per stratigraphic interval; (2) counts per million years (counts in each stratigraphic interval, divided by interval length); (3) percentages per interval (counts divided by total diversity); and (4) percentages per million years (counts divided by total diversity and interval length). This yields a total of eight data sets (two taxonomic levels times four metrics) for both extinctions and originations.

Spectral analysis shows that across all eight data sets, extinctions and originations have fundamentally different scaling behaviour (Fig. 1; and Supplementary Information). From the shortest resolvable timescale (~10 Myr, twice the average sampling interval) to the longest (~500 Myr, the length of the data set), the spectral power of extinction rates usually lies within the confidence limits for white noise, as estimated by randomly shuffling and re-analysing the

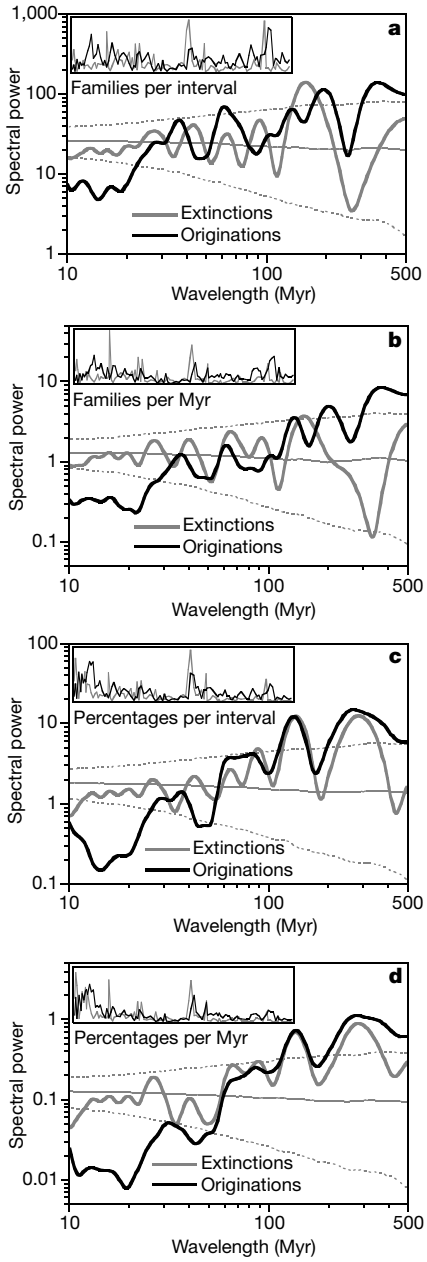

Figure 1 Fourier power spectra for extinction and origination rates of fossil marine families. Four different metrics were used: families per stratigraphic interval (**a**) and per million years (**b**), and percentages of total diversity per stratigraphic interval (**c**) and per million years (**d**). Insets show the raw time series. Spectra are smoothed over a window spanning 5% of the width of each plot. Fine lines are the median and 90% confidence limits for spectral power of random white noise at each wavelength, estimated by repeating the same analysis on 10,000 random re-shuffles of the original extinction data. Spectral power is the square of amplitude at each wavelength; thus, the relative placement of extinction and origination spectra is not arbitrary. Origination rates have markedly lower spectral power than extinction rates at wavelengths less than roughly 25 Myr, indicating that they are much less variable over short timescales. Spectra for genera are similar (see Supplementary Information).